



Catalytic oxidation for elimination of methyl bromide fumigation emissions using ceria-based catalysts



Chia-Ying Chen, Joseph J. Pignatello*

Department of Environmental Sciences, The Connecticut Agricultural Experiment Station, 123 Huntington Street, P.O. Box 1106, New Haven, CT 06504-1106, United States

ARTICLE INFO

Article history:

Received 23 November 2012
Received in revised form 26 May 2013
Accepted 18 June 2013
Available online 28 June 2013

Keywords:

Bromomethane
Fumigation
Catalytic combustion
Brominated VOCs
HBr oxidation

ABSTRACT

Methyl bromide (CH_3Br , MB) is an effective chemosterilant in quarantine and pre-shipment (QPS) chamber fumigation applications. Efficient methods to destroy or capture and reuse spent MB in QPS operations are required in view of the recognized ozone depleting potential of MB. Oxidation of 34,000 ppmv MB in simulated QPS airstreams was examined over catalysts composed of Pt, Pd, Fe_2O_3 , CuO, or PbO nanoparticles on oxide (Al_2O_3 , SiO_2 , and TiO_2) or mixed-oxide ($\text{CeO}_2\text{--Al}_2\text{O}_3$, $\text{CeO}_2\text{--SiO}_2$, and $\text{CeO}_2\text{--TiO}_2$) supports, and by self-assembled core-shell catalysts (Pd@SiO_2 and $\text{Pd@10\%CeO}_2\text{--Al}_2\text{O}_3$). The most effective support by far was ceria. The effect of noble metal doping was modest; Pt was more active than Pd in $\text{CeO}_2\text{--Al}_2\text{O}_3$ based catalysts, while Pd was more active than Pt in TiO_2 based catalysts. The most effective catalyst tested was 1%Pt/30% $\text{CeO}_2\text{--Al}_2\text{O}_3$, with 100% CeO_2 being only slightly less effective. Using 1%Pt/30% $\text{CeO}_2\text{--Al}_2\text{O}_3$, MB was completely oxidized at 400 °C, independent of airstream humidification, to give HBr as the initial product, which was subsequently oxidized to Br_2 by a Deacon-type reaction. The selectivity for Br_2 in MB decomposition increased with temperature, maximizing at ~90% at ~350 °C, and was slightly less favored in a humidified air stream. Bromide builds up on the catalyst at temperatures below 300 °C, but burns off as the temperature increases. Catalytic oxidation by ceria-based catalysts appears to be a promising approach for eliminating MB from QPS fumigation emissions.

© 2013 Elsevier B.V. All rights reserved.

1. Introduction

Methyl bromide (MB) has been widely used historically as a soil fumigant and chemosterilant for durable and fresh commodities in trade channels [1]. In 1992 MB was listed as an ozone depleting substance under the Montreal Protocol. Its use was to be phased out by 2005 in the United States and other developed countries [2], and by 2015 in developing countries [3]. However, the Montreal Protocol allows critical use exemption (CUE) [4] or quarantine and pre-shipment (QPS) exemption [5] in cases where feasible technical or economical replacements are lacking. As a result, except for a complete ban of MB use within the European Union (effective March 18, 2010) [6], MB is still in use in most countries [7] under the auspices of CUE or QPS exemptions. In typical QPS fumigations, the commodity is treated in a chamber and the spent MB vapors are then vented to the atmosphere. Development of methods to destroy or capture and reuse spent MB is urgently needed to eliminate MB emissions for environmental and health reasons, as well as to preserve the current QPS exemption for MB.

Several approaches for trapping or degrading MB vapors have been tested, but few of them are practical for dealing with chamber fumigation situations. MB emissions from soil fumigation have been transformed in a reactive layer of ammonium thiosulfate between two layers of plastic film [8], or by injecting NH_4OH beneath an impermeable film [9]. Methyl bromide undergoes nucleophilic attack by those reagents. Chamber emissions have been captured by activated carbon [10–12]. Leech et al. [10] demonstrated that activated carbon could adsorb up to 10% by weight of MB in a vent stream initially containing 16,000 parts per million by volume (ppmv) MB (average concentration, 3800 ppmv). Later, Snyder and Leesch combined activated carbon adsorption with electrothermal regeneration [11]. Gan and Yates [12] captured and decomposed MB in a slurry of activated carbon in sodium thiosulfate solution; decomposition required from 0.5 to 9 h at 20 °C. The addition of triethylene diamine (TEDA) to coconut shell activated carbon was reported to increase MB breakthrough time and result in methylation of TEDA by MB, but the overall removal capability of MB was adversely affected by humidity [13]. Despite the limited successes of these methods, none of them has been able to reach widespread use. This may be due to practical or economic obstacles, such as slow reaction, adsorptive competition by water vapor, or additional costs to dispose or regenerate the adsorbent. With these considerations, further research on

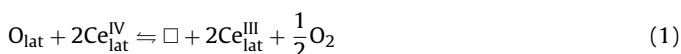
* Corresponding author. Tel.: +1 2039748518.

E-mail addresses: joseph.pignatello@ct.gov, joseph.pignatello@yale.edu (J.J. Pignatello).

novel methods to destroy or capture and reuse spent MB is warranted.

The removal of hazardous volatile organic compounds (VOCs) and gases such as CO, SO_x and NO_x from exhaust streams is required in automobile operation and many industrial processes. One of the most effective techniques is catalytic oxidation, in which a solid catalyst is employed to lower the temperature of thermal oxidation, often by several hundred degrees [14,15]. Three main types of combustion catalysts for VOCs have been studied: supported noble metals [16,17], transition metal oxides [18,19], and zeolites [20,21]. Halogenated VOCs (HVOs) have received relatively little attention compared to non-halogenated VOCs. Catalytic oxidation seems a promising alternative for removal of MB because it uses “free” reagents (air) and is expected to convert MB instantly and completely to inorganic products.

Ceria (CeO₂) has been widely used as a promoter when added to high surface area supports such as Al₂O₃ and SiO₂. Ceria is a central component of catalysts used in the treatment of automobile exhausts, removal of SO_x and NO_x from flue gases, and selective oxidation reactions [22]. Relative to other oxide supports, ceria improves catalyst performance by inhibiting sintering of noble elements [23], promoting dispersion of noble metals on the support [24], facilitating noble metal reduction and oxidation [22], increasing thermal stability of co-components [25], and increasing overall catalytic efficiency in mixtures with other oxide supports [26–29]. Moreover, ceria has higher intrinsic catalytic activity than other supports. A key property of ceria is its ability to form a continuum of oxygen-deficient, nonstoichiometric oxides (CeO_{2-x}; 0 < x ≤ 0.5), while retaining its (fluorite) crystal structure (Eq. (1)),



where O_{lat} is lattice oxygen, Ce_{lat}^{IV} is normal lattice cerium, □ is a lattice oxygen vacancy and Ce_{lat}^{III} is the reduced form of lattice Ce. This reaction is reversible [22], so that ceria acts as an oxygen storage material in catalyzed oxidations [30]. Noble metals (Pt, Pd or Rh) promote reduction of Ce_{lat}^{IV} to Ce_{lat}^{III} and increase oxygen storage capacity [31,32]. Addition of ceria to (Pt, Pd, or Rh)/Al₂O₃ appears to decrease the activation energy for oxidation of CO and HCs [32]. Vacancies and “active” oxygen involved in the pathway of reaction 1 are believed to play roles in the oxidation of VOCs and other gases [22,30].

Oxidation of hydrocarbons (HCs) over ceria-based catalysts is thought to proceed by the Mars-van Krevelen redox cycle, in which the first step is hydrogen abstraction by a coordinatively unsaturated active surface lattice oxygen, O_{lat}^{*}, giving CO₂ and H₂O, which desorb, exposing vacancies that are replenished by gas-phase dioxygen [29,33]:



where β is the stoichiometric ratio forming product P. The combustion of methane over Pd oxide-based catalysts has been studied in great detail and likely proceeds similarly [34]. The participation of lattice oxygen species in HCl oxidation on metal oxides can also be supported experimentally by temporal-analysis-of-products technique [35]. Whether step 3 or some other step is central to HVOC oxidation has not been established. In some cases, Lewis acid–base chemistry is likely involved, as chloroethene is an intermediate of 1,2-dichloroethane oxidation catalyzed by ceria and ceria–zirconia mixed oxides [36].

While the high activity of CeO₂ catalysts toward other VOCs and HVOs is known, there are no reports on the combustion of MB using CeO₂-based catalysts. In fact, the only report to our knowledge on catalyzed thermal oxidation of MB is one by Window and Zhang [17], who published the ignition curves of MB over Pt/Al₂O₃ and Pt/TiO₂ in the course of addressing the competitive effect of MB on toluene oxidation. One objective of our study was to screen CeO₂-based and other supported oxide catalysts for activity toward MB in air streams simulating vent streams from QPS chamber fumigations. A second was to shed some light on the reaction mechanism using the most active catalyst found.

2. Experimental

2.1. Catalyst preparation

Catalysts prepared by wet impregnation. Catalysts of Pt, Pd, Fe₂O₃, CuO, and PbO on oxide supports, Al₂O₃, SiO₂, and TiO₂, and mixed oxide supports, CeO₂–Al₂O₃, CeO₂–SiO₂, and CeO₂–TiO₂, were prepared via wet impregnation [29,37]. Hydrogen hexachloroplatinate (H₂Cl₆Pt·6H₂O, Acros Organics, 99.90%), potassium tetrachloropalladate (K₂PdCl₄, Acros Organics, Pd ≥ 32%), ferric nitrate (Fe(NO₃)₃·9H₂O, Mallinckrodt Chemical Works, 99%), copper nitrate (Cu(NO₃)₂·3H₂O, Mallinckrodt Chemical Works, 99.9%), lead nitrate (Pb(NO₃)₂, Fisher Scientific, 99.95%), and cerium nitrate (Ce(NO₃)₃·6H₂O, Acros Organics, 99.5%) were used as metal precursors, while Al₂O₃ (Fisher Scientific), TiO₂ (Sigma–Aldrich, ≥99%), SiO₂ (Spectrum Chemical Manufacturing Corp.), and CeO₂ (Acros Organics, 99.9%) were used as supports. The mixed oxide supports were prepared by adding Al₂O₃, SiO₂, or TiO₂ to aqueous solutions (100 mL) of cerium nitrate and mixing for 3 h. The product was dried at 110 °C for 24 h and then calcined in air at 500 °C for 5 h. Noble metal (1% Pt or Pd) or metal oxide dopants (5% Fe₂O₃, CuO, and PbO) were incorporated into the prepared mixed oxides (CeO₂–Al₂O₃, CeO₂–SiO₂, and CeO₂–TiO₂) or commercial oxides (Al₂O₃ and TiO₂) by the same mixing, drying, and calcination techniques. Weight percent was used unless specified.

Core–shell catalysts. This group includes Pd@SiO₂ and Pd@10%CeO₂–Al₂O₃. They were prepared in an identical manner as reported by Forman et al. [38] and Cargnello et al. [39], respectively. For preparing Pd@SiO₂, a mixture of tetraethyl orthosilicate and *n*-octadecyl trimethoxysilane was employed as the SiO₂ precursor, and hydrazine was used as the reducing agent. Pd@SiO₂ was precipitated, centrifuged and washed in ethanol, followed by drying and then calcining at 550 °C in air for 6 h. The Pd@10%CeO₂–Al₂O₃ was prepared by adding Al₂O₃ to synthesized Pd@CeO₂ which was prepared by exploiting the self-assembly between 11-mercaptopundecanoic acid-functionalized Pd nanoparticles and cerium decyloxyde. After recovery from THF, the Pd@10%CeO₂–Al₂O₃ was dried and calcined at 500 °C for 5 h.

2.2. Catalyst characterization

Surface area was determined by gas adsorption on an Autosorb-1 gas analyzer (Quantachrome Instrument Corp., Boynton Beach, FL) after outgassing at 200 °C, by application of the Brunauer–Emmett–Teller (BET) equation to an 11-point adsorption isotherm of N₂ at 77 K in the region 0.05–0.3 relative pressure. Metal loading was analyzed using Inductively Coupled Plasma Optical Emission Spectrometry by Galbraith Laboratories, Knoxville, TN. Powder X-ray diffraction (XRD) patterns were recorded on a Bruker AXS D8Focus diffractometer using a Ni-filtered Cu Kα radiation (λ = 0.154061 nm), and operating at 40 kV and 40 mA. Diffraction data were collected between 20° and 80° (2θ) with a resolution of 0.05° (2θ). Structural morphology was investigated

by high-resolution transmission electron microscopy (HRTEM) and high-angle annular dark-field (HAADF) imaging/energy dispersive X-ray spectroscopy (EDS) mapping in the scanning transmission electron microscopy (STEM) mode. A FEI Tecnai Osiris 200 kV microscope was used. Samples were mounted on standard grids with a holey-carbon film. The surface elemental composition was determined by X-ray photoelectron spectroscopy (XPS). Data were collected using a ThermoScientific ESCALAB 250 instrument with a monochromatized Al X-ray source at the University of Oregon CAM-COR facility. High resolution spectra of the Ce 3d, Pt 4d, Al 2p, Br 3p, O 1s, and C 1s core level regions were recorded with pass energy of 50 eV and a spectral acquisition time of 15 min. The BEs were estimated with an accuracy of ± 0.2 eV. Peak fitting was performed with Avantage software provided by Thermo Electron Corporation, using a Shirley type background subtraction and assuming Gaussian/Lorentzian peak shapes.

2.3. Catalyst performance tests

Catalyst performance was tested using a continuous flow fixed-bed quartz reactor (Fig. S1). A constant flow of air or nitrogen at $0.15 \text{ LSTP min}^{-1}$, either hydrated by passing through a water bubbler or dehydrated by passing through a CaSO_4 column, was mixed with MB (100%; Cardinal Professional Products, Hollister, CA) to achieve $\sim 3.4 \times 10^4 \text{ ppmv}$, a concentration typically found in gases initially vented from QPS fumigation chambers. Condensation of MB in the tubing just outside its gas cylinder was prevented by warming the cylinder and the tubing in a water bath to 38°C , and by surrounding the section of tubing between the water bath and the gas mixer with a warmed heating tape. The gas stream was conveyed through stainless steel tubing and/or Teflon connectors to a tubular quartz reactor (i.d. = 0.94 cm) fitted with a quartz frit to retain the catalyst. The reactor was housed in a 5 cm diameter by 15 cm long electrically heated ceramic heater. Catalyst (0.1 g) was packed at the bed of the reactor, resulting in constant space time $(W/F^\circ(\text{MB})) = 7.7 \text{ g h mol}^{-1}$, defined as the ratio of the catalyst mass to the inlet molar flow of MB.

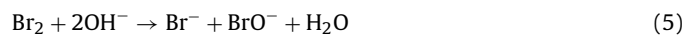
Passage of HBr or Br_2 through the reactor in the presence or absence of catalyst (0.1 g) was accomplished by replacing the water in the water bubbler with 48% HBr (Sigma–Aldrich) or a mixture of water and neat Br_2 (Sigma–Aldrich, $\geq 99.99\%$), respectively, using a constant flow of air at $0.15 \text{ LSTP min}^{-1}$.

2.4. Analysis of methyl bromide

MB in the effluent gases from the reactor was measured on-line with an Agilent 6890 gas chromatograph equipped with a 6-port gas sampling valve with a $250 \mu\text{L}$ sample loop and a flame ionization detector (FID). The gas samples were injected by the splitless technique onto an Agilent GS-Q PLOT column ($30 \text{ m} \times 0.535 \text{ mm}$) with $20 \text{ mL min}^{-1} \text{ H}_2$ carrier gas. The injection port, oven, and FID temperatures were 150°C , 100°C , and 300°C , respectively. Under these conditions, the retention time of MB was 2 min .

2.5. Analysis of products

Bromine products in the reactor effluent gases were trapped by a solution of 0.0125 N NaOH in a bubbler placed downstream from the reactor. Bromine was determined from the hypobromite ion produced in the trapping solution, taking into account the reaction stoichiometry:



Hypobromite concentration was determined by titration with ferrous ammonium sulphate (Sigma–Aldrich, $\geq 98\%$), using *N,N*-diethyl-*p*-phenylenediamine (Acros Organics, 99%) as indicator

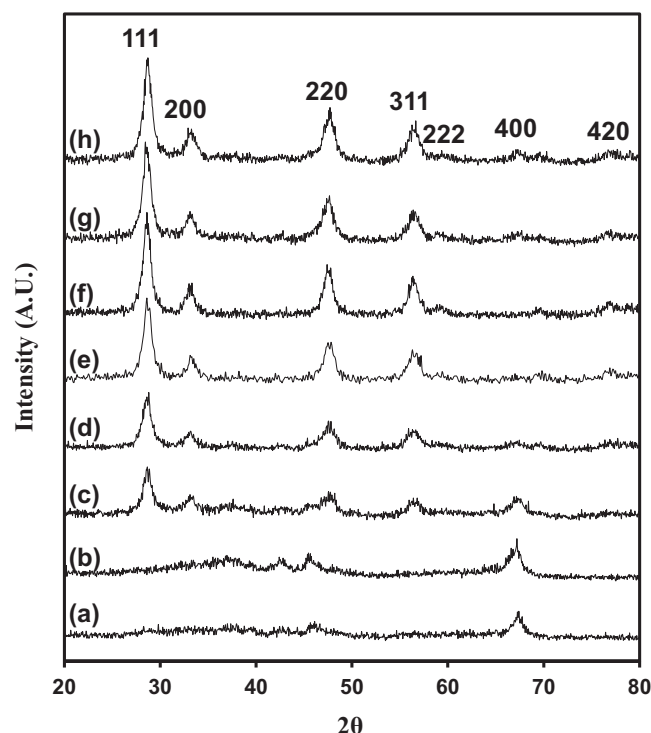


Fig. 1. X-ray diffraction patterns of synthesized catalysts: (a) Pd@10%CeO₂–Al₂O₃; CeO₂–Al₂O₃ with various ceria contents (weight percent): (b) 0, (c) 10, (d) 30, (e) 50, (f) 100, (g) Pt/30%CeO₂–Al₂O₃, and (h) Pd/30%CeO₂–Al₂O₃.

[40] and based on calibration curves from solutions freshly-prepared from Br_2 in NaOH solution. The yield of bromide in the trap fluid attributable to MB oxidation was taken to be the observed bromide ion minus the bromide ion generated via eq 5. Bromate ion may form from the hypobromite ion produced: $3\text{BrO}^- \rightarrow 2\text{Br}^- + \text{BrO}_3^-$ [41]. Bromide and bromate ion concentrations were measured by ion chromatography on an IonPac AS4A analytical column ($250 \text{ mm} \times 4 \text{ mm I.D.}$, $16 \mu\text{m}$ particle size, DIONEX Corporation) using sodium carbonate and sodium bicarbonate as eluent at 2 mL min^{-1} .

3. Results and discussion

3.1. Catalysts properties

The XRD patterns of the selected catalysts shown in Fig. 1 are in accord with the literature. The $\gamma\text{-Al}_2\text{O}_3$ support gives broad diffraction peaks, ascribed to the defective spinel structure with Al cations occupying the Al and Mg sites, and the intensity weakens as ceria content exceeds 10%. The spectrum of 100% ceria shows sharp and distinct diffraction peaks. The Bragg peaks with Miller indices (1 1 1), (2 0 0), (2 2 0), (3 1 1), (2 2 2), (4 0 0), (4 2 0) indicate the formation of a cubic fluorite-like lattice of pure CeO₂ (JCPDS No. 34-0394) [42]. The diffraction peaks of ceria increase in prominence with an increase in ceria content, consistent with the results of Abbasi et al. [29]. The ionic radius of Al(III) is smaller than that of Ce(IV) [43]; thus, the incorporation of Al(III) into the ceria lattice results in decreased crystal size and broader peaks. The stronger peaks of Pd/30%CeO₂–Al₂O₃ and Pt/30%CeO₂–Al₂O₃ compared to 30%CeO₂–Al₂O₃ in Fig. 1 can be attributed to the doubled calcination time used. No diffraction of platinum or palladium oxide appear in the samples (Fig. 1(g) and (h)), meaning no large PdO and PtO crystals were formed, indicating high dispersion of the noble metal species.

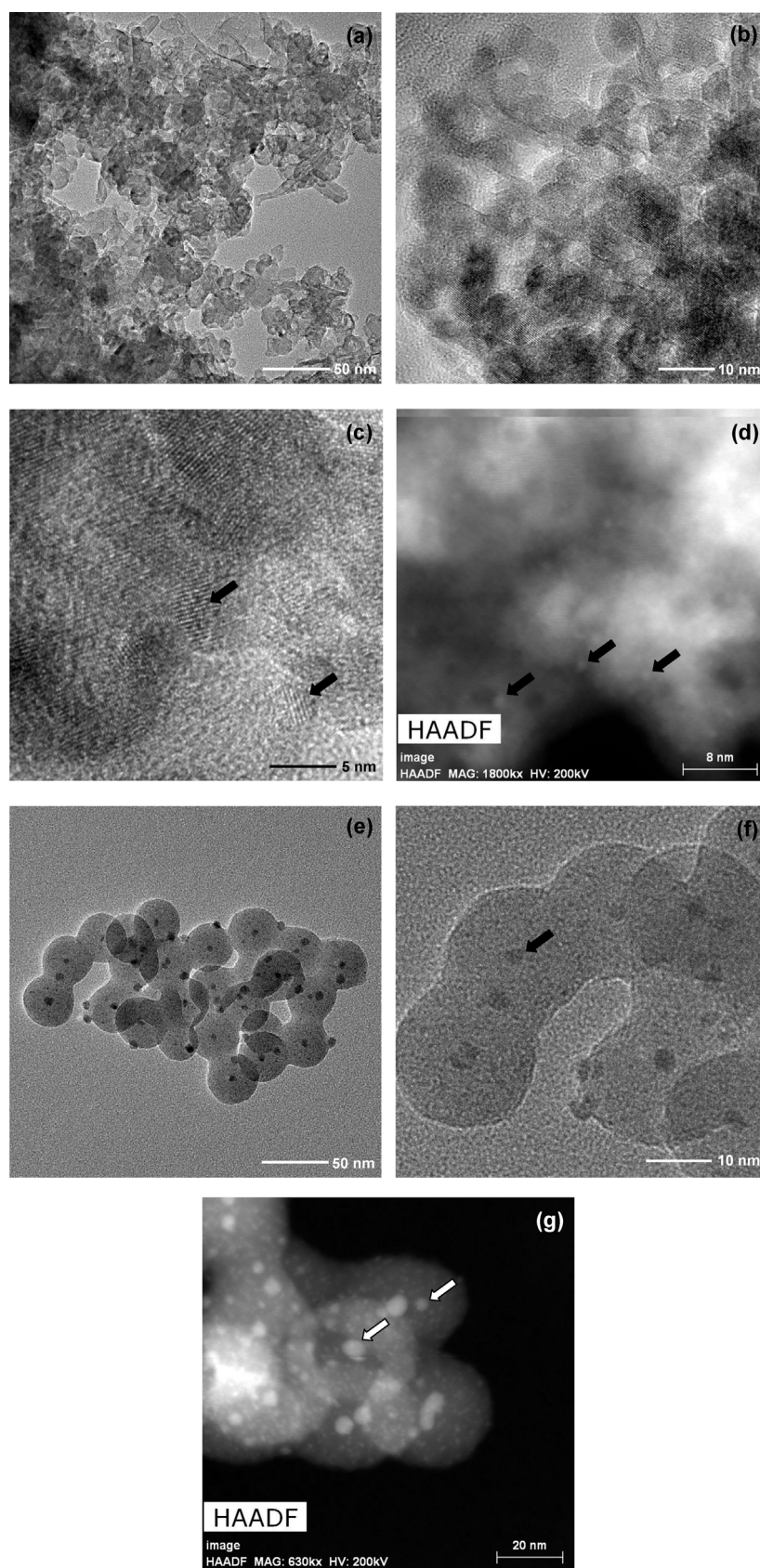


Fig. 2. TEM and STEM images of Pt/30%CeO₂-Al₂O₃ (a–d) and Pd@SiO₂ (e–g). Note arrows point to Pt or Pd particles.

Table 1

Crystal size and specific surface area of selected catalysts.

Catalyst	Crystal size (nm) ^a	BET surface area (m ² /g)	Noble metal loading (wt%)
CeO ₂ –Al ₂ O ₃	7.19	98.9	–
Pt/30%CeO ₂ –Al ₂ O ₃	7.76	91.7	0.925
Pd/30%CeO ₂ –Al ₂ O ₃	8.11	90.5	0.969
Pd@10%CeO ₂ –Al ₂ O ₃		128	0.314
Pd@SiO ₂		78.1	5.32

^a Crystal sizes were calculated from (1 1 1) crystal plane by the Scherrer equation.

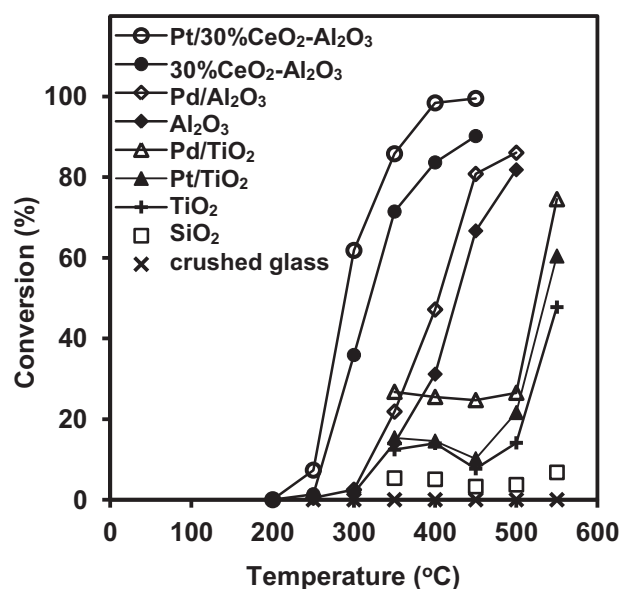
Crystal size, BET specific surface area, and noble metal content (wt%) are listed in Table 1. Crystal sizes of Pt/30%CeO₂–Al₂O₃ and Pd/30%CeO₂–Al₂O₃ calculated from (1 1 1) crystal plane by the Scherrer equation are about 7–8 nm. The surface areas of Pt/30%CeO₂–Al₂O₃, Pd/30%CeO₂–Al₂O₃, and 30%CeO₂–Al₂O₃ are 91.7, 90.5, and 98.9 m²/g respectively. The slightly larger surface area of 30%CeO₂–Al₂O₃ is in line with its smaller crystal size.

Transmission electron microscopy (TEM) and high-angle annular dark-field (HAADF) imaging in the scanning transmission electron microscopy (STEM) mode were performed to investigate the morphology and microstructure of synthesized catalysts. The strong correlation of image contrast to the atomic mass in HAADF-STEM helps characterize and locate heavy metals on nanoscale particles, as the HAADF-STEM image becomes brighter as the element's atomic mass increases [44]. Fig. 2(a) and (b) shows the support particle size of Pt/30%CeO₂–Al₂O₃ is ~7–8 nm, in line with the CeO₂ crystal sizes calculated by the Scherrer equation in XRD spectrum (Table 1). Pt particles are well dispersed on the surface with a homogeneous size distribution centered at 2 nm (Fig. 2(c) and (d)). The corresponding spatial distribution of Pt, Ce, and Al using energy dispersive X-ray spectroscopy (EDS) mapping on HAADF-STEM image (Fig. S2(b)) offers confirmation of the presence and good dispersity of Pt nanoparticles along the surface. For Pd@SiO₂ core-shell particles, TEM (Fig. 2(e) and (f)), as well as HAADF-STEM image (Fig. 2(g)) and EDS mapping (Fig. S2(d)) clearly show the SiO₂ shells are approximately 10 nm in thickness, and Pd particles are within and on the surface of the silica walls. Both uniform shape and monodispersed size were observed for SiO₂ shells and Pd cores.

3.2. Catalyst activity

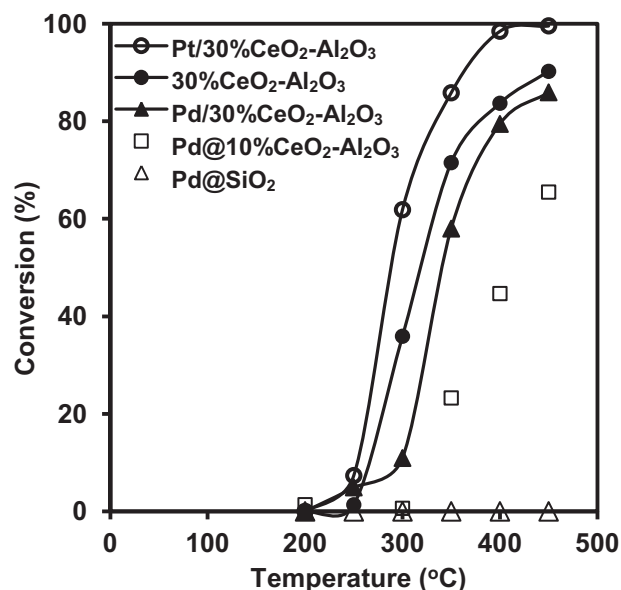
Various catalysts were screened for activity and the results are shown in Figs. 3–5. No conversion of MB occurred with 100 mg 60-mesh crushed borosilicate glass up to 550 °C (Fig. 3). The nature of the support has a clear effect on catalyst activity. The activity of the oxide support follows the order, CeO₂–Al₂O₃ mixtures > Al₂O₃ > TiO₂ >> SiO₂ (no activity up to 550 °C). This trend is consistent with that of a previous study of toluene oxidation over supported copper oxide catalysts: Cu/CeO₂ > Cu/γ-Al₂O₃ > Cu/TiO₂ [27]. The activity of all TiO₂ supported catalysts plateaued in the 10–30% range between 350 and 500 °C, and then increased sharply as the temperature rose above 500 °C.

The addition of noble metals (e.g., Pd or Pt) generally enhanced activity, but not dramatically. The Al₂O₃ supported catalysts, Pd/Al₂O₃ and Al₂O₃ reached 86 and 82% efficiency, respectively, at 500 °C. Among the TiO₂ catalysts, activity followed the order, Pd/TiO₂ > Pt/TiO₂ > TiO₂. The catalysts Pt/30%CeO₂–Al₂O₃, 30%CeO₂–Al₂O₃, and Pd/30%CeO₂–Al₂O₃ gave 98%, 84%, and 80% conversion of MB, respectively, at 400 °C (Fig. 4). The order in activity for the noble metal-doped 30%CeO₂–Al₂O₃ catalysts is Pt > Pd, the opposite of that for the noble metal-doped titania catalysts (Fig. 3). This is consistent with a recent study of perchloroethylene [28], which found that Pt > Pd on CeO₂–Al₂O₃ and Al₂O₃ supports, whereas Pd > Pt on Al₂O₃–TiO₂ supports, and which was attributed

**Fig. 3.** Catalytic conversion of methyl bromide versus temperature over synthesized catalysts on different supports.

to the redox cycling behavior of the noble metal on the different surfaces. Note the presence of noble metals was reported to lower the Ce-reduction temperature and increase the oxygen storage capacity (OSC) of CeO₂ [31]. The OSC in precious metal-containing mixed-oxide catalysts (Pt, Pd, and Rh)/CeO₂–Al₂O₃ is found to be much higher than the OSC in CeO₂–Al₂O₃ and precious metals/CeO₂ catalysts [31]. Also, addition of Pt to CeO₂ and CeO₂–ZrO₂ significantly improves migration of oxygen in the support [45]. Indeed, the results of Fig. 2 and Fig. S2 indicate a mutual benefit of Pt and CeO₂; namely, that Pt promotes dispersion of CeO₂ on alumina, and that CeO₂ promotes dispersion of Pt on the support.

Of two core-shell catalysts tested, Pd@10%CeO₂–Al₂O₃ showed low activity (i.e. 45% conversion at 400 °C), and Pd@SiO₂ showed no activity. The low activity of Pd@10%CeO₂–Al₂O₃ may be attributed to agglomeration of hydrophobic Pd@CeO₂ structures on the highly hydrophilic alumina support [46]. For Pd@SiO₂, some of the Pd

**Fig. 4.** Catalytic conversion of MB over synthesized Pt/30%CeO₂–Al₂O₃, 30%CeO₂–Al₂O₃, Pd/30%CeO₂–Al₂O₃, Pd@10%CeO₂–Al₂O₃, and Pd@SiO₂.

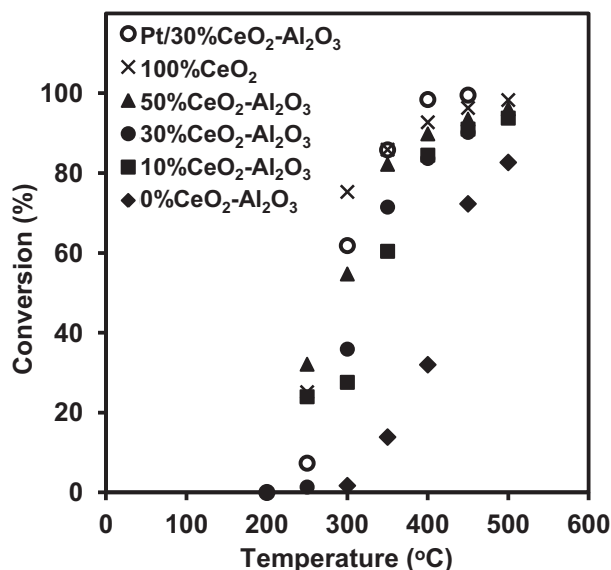


Fig. 5. Catalytic conversion of methyl bromide over synthesized $\text{CeO}_2\text{-Al}_2\text{O}_3$ catalysts with different ceria contents.

nanoparticles are uniformly dispersed on the surface (Fig. 2), so the lack of activity of Pd@SiO_2 is more likely due to the general inertness of the SiO_2 support as shown in Fig. 3.

CeO_2 is clearly superior among the supports tested due to the earlier-mentioned properties of ceria [22]. The addition of 30% ceria to Al_2O_3 greatly improved activity relative to Al_2O_3 alone. The activity of catalysts with ceria contents of 0, 10, 30, 50, and 100% (the remainder Al_2O_3) increases with increasing fraction of ceria (Fig. 5). Similar results were reported in the oxidation of propene and toluene by various gold-supported catalysts, whose activity followed the sequence (1.5% nanoparticulate Au in each case): $\text{Au/CeO}_2 > \text{Au/7.5\%Ce/Al}_2\text{O}_3 > \text{Au/Al}_2\text{O}_3$ [26]. The authors attributed this trend to the presence of structural defects in ceria, which increase lattice oxygen mobility and decrease gold particle size due to anchoring of gold on the ceria. The 100% CeO_2 catalyst was slightly less active than 1% $\text{Pt/30\%CeO}_2\text{-Al}_2\text{O}_3$. But note that $\text{Pt/30\%CeO}_2\text{-Al}_2\text{O}_3$ is considerably more active than 30% $\text{CeO}_2\text{-Al}_2\text{O}_3$, signifying the positive role of Pt. It is possible also that metal dopants may improve selectivity for CO_2 over CO, as has been reported (e.g., Cu [27] and Pt and Pd [47]). We did not monitor CO_2 and CO here. Also, the formation of Pt–O–Ce surface complex may increase resistance to sintering.

Doping 30% $\text{CeO}_2\text{-Al}_2\text{O}_3$ with 5% of Fe, Cu or Pb oxides (Fig. S3(a)) generally reduced activity but only slightly. The activity of the co-support of the 30% CeO_2 -mixed oxides follows the order $\text{-Al}_2\text{O}_3 > \text{-SiO}_2 \sim \text{-TiO}_2$ (Fig. S3(b)), but the differences are only slight. This, together with the effect of increasing ceria content of $\text{CeO}_2\text{-Al}_2\text{O}_3$ mixed oxides in Fig. 5, and the only modest enhancement by noble metals, shows that ceria itself plays a predominant role in MB oxidation in all the catalysts containing ceria.

The most active catalyst found so far, $\text{Pt/30\%CeO}_2\text{-Al}_2\text{O}_3$, was tested under different conditions. The catalyst was inactive under pure nitrogen flow for 3 h at both 350 °C and 400 °C. In air, conversion occurred to an indential degree in the absence or presence of water vapor initially at near 100% relative humidity just before entering the heated zone. Moisture at high levels is always present in QPS vent gases. No methanol was detected in the MB effluent vapor. Together, these results show that catalysis occurs by a redox pathway, not by hydrolysis or Lewis acid–base catalysis. Moisture also had no reported effect on $\text{Pt/Al}_2\text{O}_3$ catalyzed conversion of chloroform and dichloromethane [16]. The $\text{Pt/30\%CeO}_2\text{-Al}_2\text{O}_3$

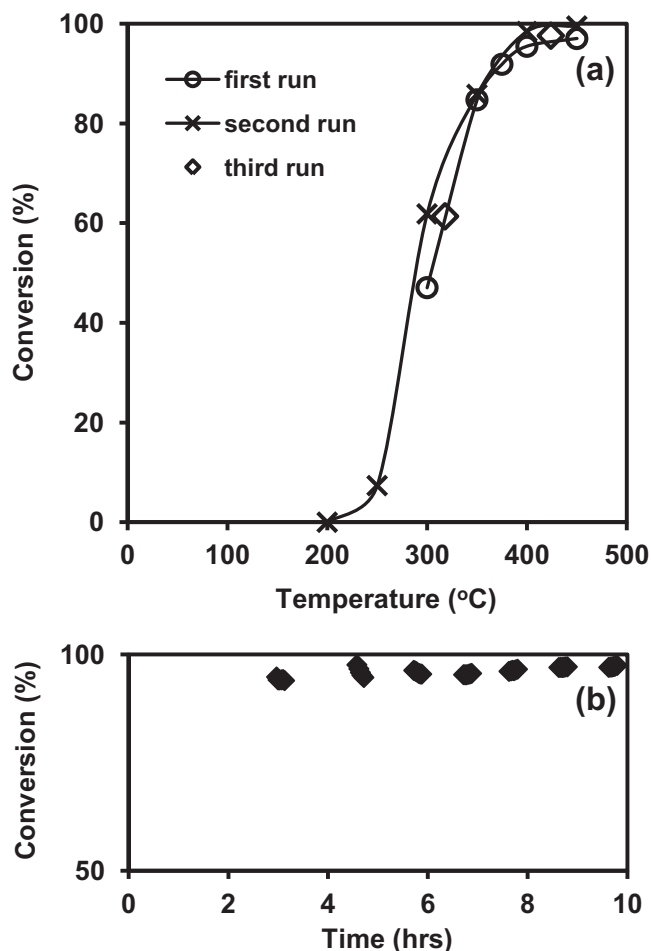
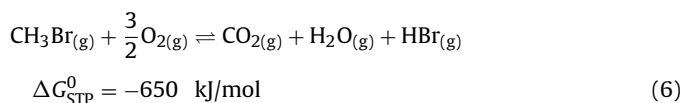


Fig. 6. Endurance test of catalytic conversion of MB over $\text{Pt/30\%CeO}_2\text{-Al}_2\text{O}_3$ (a) during three consecutive runs, and (b) a function of time-on-stream for 10 h continuous operation at 400 °C.

catalyst shows no deactivation after three consecutive runs corresponding to a total of about 57 min exposure of the catalyst to temperatures at or above 300 °C (Fig. 6(a)), as well as continuous time-on-stream operation at 400 °C for 10 h (Fig. 6(b)). This suggests that the developed catalyst has great endurance under our conditions, in which reactive bromine products are formed (see Section 3.3). By comparing the XRD patterns of fresh and used samples after exposure to MB at both 400 °C for 10 h or 275 °C for 7 h (Fig. S4), no detectable phase variations were observed. This indicates there is no detectable bulk bromination at both temperatures. At 400 °C, this is quite as expected, since MB should be oxidized completely at 400 °C according to Fig. 7. The absence of Br in the bulk catalyst state could also be due to the inability of Br to diffuse through the crystal. Similarly, CeO_2 does not display bulk chlorination in HCl oxidation at 450 °C under O_2 -rich conditions [34]. Later, we show Br in the near surface region of used catalysts by XPS.

3.3. Products and pathways for $\text{Pt/30\%CeO}_2\text{-Al}_2\text{O}_3$

Both Br_2 and HBr were produced from MB, their yields dependent on temperature (Fig. 7). The possible net reactions are:



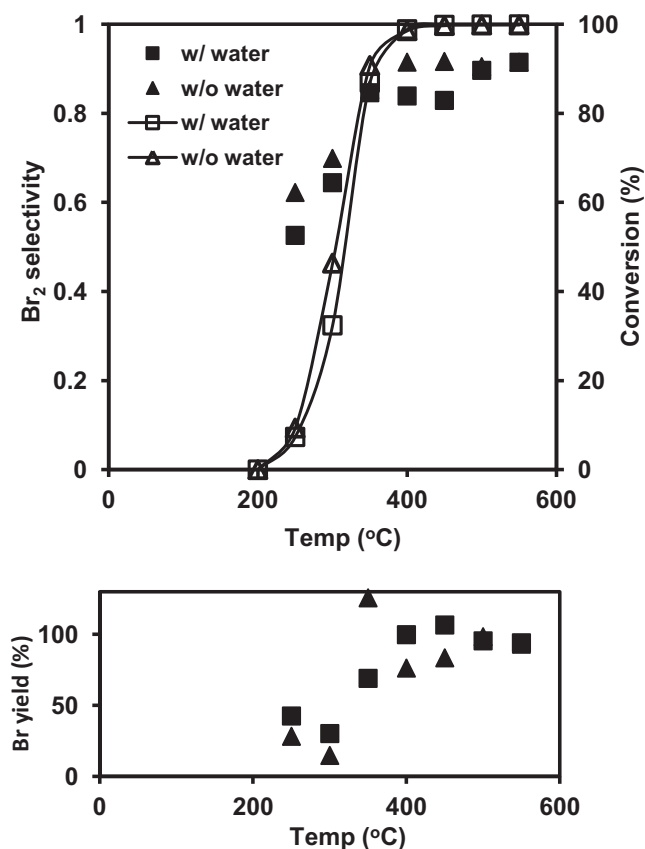
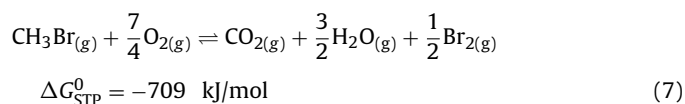


Fig. 7. Br₂ selectivity in the effluent, catalytic conversion of MB, and total Br yield ($2\text{Br}_2 + \text{HBr} \times 100\% / (\text{CH}_3\text{Br consumed})$) over Pt/30%CeO₂–Al₂O₃ in the presence (squares) or absence (triangles) of moisture. For the upper graph, open symbols represent conversion and filled symbols represent Br₂ selectivity.



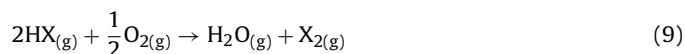
Reaction (7) is more thermodynamically favorable than reaction (6) at standard temperature and pressure (STP), and likely so up to several hundred °C.

The molar selectivity for Br₂ is defined as,

$$S = \frac{2 \cdot \text{Br}_2}{2 \cdot \text{Br}_2 + \text{HBr}} \quad (8)$$

Bromine selectivity based on the amounts of Br₂ and HBr collected in the post-reactor NaOH trap is shown as a function of heating temperature in Fig. 7. The reaction becomes increasingly selective for Br₂ with temperature and percent conversion of MB. Likewise, oxidation of both 1,2-dichloroethane and trichloroethylene catalyzed by Ce-rich mixed oxides becomes more selective for Cl₂ at the expense of HCl with temperature and conversion [36]. MB oxidation is moderately less selective for Br₂ in humidified air than dry air over most of the temperature range.

Bromine may be produced either directly from oxidation of MB or indirectly from oxidation of HBr via a Deacon-type reaction [48] (Eq. (9)):



The Deacon reaction for HCl is catalyzed by ceria nanoparticles [49], among other catalysts (Cr₂O₃, MnO₂, CuO, and RuO₂) [34]. The HBr Deacon-type reaction is thermodynamically more favorable than the HCl Deacon reaction ($\Delta G_{\text{STP}}^0 = -119 \text{ kJ/mol}$ for Br and -38.0 kJ/mol for Cl). There is little available information on the

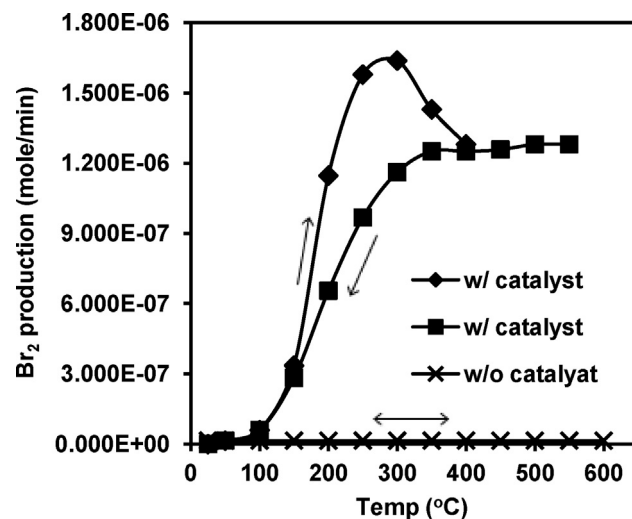


Fig. 8. Br₂ production from HBr conversion versus temperature in the presence or absence of Pt/30%CeO₂–Al₂O₃. Quantitative conversion corresponds to $1.28 \times 10^{-6} \text{ mol/min}$.

HBr Deacon-type reaction in the patent and scientific literatures [50].

The involvement of the Deacon-type reaction in MB oxidation was evaluated by passing moist HBr vapor through the continuous flow fixed bed reactor in the presence or absence of Pt/30%CeO₂–Al₂O₃ (Fig. 8). No HBr conversion took place in the absence of catalyst up to 600 °C. In the presence of this catalyst and in the 'reverse' direction (i.e. with decreasing temperature), HBr was converted to Br₂, giving a light-off point at ~200 °C and reaching 100% of theoretical yield at ~350 °C. While theoretically reversible, the catalyzed Deacon-type reaction lies far to the right of Eq. (9), as no HBr was recovered in the scrubbing liquid after passing pure Br₂ in humidified air through the reactor at 200 °C or 450 °C (see below, however). Given the active role of ceria in HBr oxidation and the coincidence of the maxima for Br₂ yield from HBr (Fig. 8) and for the Br₂ selectivity from MB (Fig. 7) (namely, ~350 °C), the results are consistent with the source of Br₂ being HBr via the Deacon-type reaction, rather than MB directly.

The conversion of HBr to Br₂ in the experiment represented in Fig. 8 was steady over the course of 9 h of continuous reactor operation at various temperatures up to 600 °C, attesting to the stability of the catalyst under harsh conditions. Likewise, conversion of HCl by 100% CeO₂ was stable over the course of three hours in a previous study [49].

The yield of total Br from MB trapped from the effluent gas was non-stoichiometric at lower temperatures but approached stoichiometric above 350 °C (Fig. 7). Extraction of the catalyst and reactor parts (walls and exit tubing) with dilute NaOH after combustion of MB at 300 °C or 450 °C recovered significant amounts of bromide ion (Table 2) but no Br₂. Recovery of bromide ion was much greater from the catalyst than from the reactor parts, and much greater at 300 °C than at 450 °C. To explain these results we return attention to the HBr conversion curve in Fig. 8, which shows hysteresis. The curve constructed in the 'forward' direction (i.e. with progressing temperature) peaks at a conversion greater than the stoichiometric ratio, whereas the curve constructed in the 'reverse' direction follows monotonically from quantitative yield to zero yield. Evidently, in the forward direction, Br (as bromide) accumulates on the catalyst at lower temperatures and, as the temperature is raised, the accumulated Br converts to Br₂ along with the incoming HBr, resulting in stoichiometric excess at the intermediate temperatures. This also explains the larger extractable bromide ion concentration from the catalyst after MB combustion at 300 °C compared to 450 °C

Table 2Yield of Br-containing species from MB conversion at 300 and 450 °C over Pt/30%CeO₂–Al₂O₃ for 10 min.

	Br [−] (catalyst extract)/MB _{consumed} ^a %	Br ₂ selectivity ^b (a)	Corr. Br ₂ selectivity ^c (b)	(a) – (b)	Br yield ^b % (c)	Corr. Br yield ^c % (d)	(c) – (d)
Humid air							
300	3.67	0.523	0.446	0.077	31.3	36.7	−5.41
450	0.477	0.873	0.865	0.009	100	101	−1.00
Dry air							
300	2.21	0.566	0.502	0.063	18.7	21.1	−2.36
450	0.429	0.944	0.937	0.007	81.0	81.6	−0.59

^a Extractable moles of Br[−] on catalyst normalized to moles MB consumed.^b Based on amounts found in NaOH_{aq} trap solution only.^c Based on amounts found in NaOH_{aq} trap solution plus amounts extracted from the catalyst and reactor parts.

(Table 2). Bromide also was extracted from the catalyst by dilute NaOH after Br₂ was passed through the reactor at 300 °C and then 450 °C, but in small yield (2.0% mol yield based on total Br₂). This implies that the HBr Deacon-type reaction may be microscopically reversible, albeit lying far to the right of Eq. (9).

When the bromide recovered from the catalyst and reactor parts is taken into account, the total Br yield from MB oxidation at 300 °C is increased only modestly (from 31.3 to 36.7% in humidified air, and from 18.7 to 21.1% in dry air), yet still does not approach stoichiometry (Table 2). Another possible Br product is bromate (BrO₃[−]), but the concentration of bromate in the trap fluid, catalyst and reactor parts was below the method detection limit, which corresponds to a molar yield of less than 0.3% yield based on MB consumed. Evidently, the nonstoichiometry observed at low MB conversion is due to bromide retention on the catalyst in a form that is incompletely extracted by dilute NaOH.

The two major Br-containing products are HBr and Br₂ – the former catalytically converted irreversibly to the latter with increasing temperature. The first Br product to leave the catalyst must, therefore, be Br(−I) and not Br(0), which cannot be efficiently reduced under the conditions. Although Br₂ is the thermodynamically favored product (Eqs. (6) and (7)), evidently HBr is the initial product of MB for kinetic reasons. Some of the bromide accumulates on the catalyst especially at lower temperature. Extractable bromide is also found on the catalyst in the reverse Deacon-type reaction, as noted above. Previous work [49] indicates that vacancies rather than active lattice oxygen play the critical role in CeO₂-catalyzed oxidation of HCl. Thus, MB and HBr oxidation may utilize different active sites on the catalyst. Amrute et al. [49] spectroscopically observed Cl incorporation into ceria in the upper 1–1.5 catalyst layers at low O₂/HCl ratios (0–0.75) in the feed stream. They suggested that Cl[−] occupies vacancies and CeCl₃-like bulk phases. Similarly, Br[−] may occupy vacancies and CeBr₃-like phases. And, like Cl[−] [49], Br[−] probably cannot penetrate far into the bulk ceria. The surface elemental composition was then determined by XPS spectroscopy.

XPS was performed to determine the surface elemental composition of Pt/30%CeO₂–Al₂O₃ unused (“fresh”), after exposure to MB at 400 °C for 10 h (“400 °C–MB–10 h”), after exposure to MB at 275 °C for 7 h (“275 °C–MB–7 h”), and after exposure to HBr at 250 °C for 7 h (“250 °C–HBr–7 h”). Their Ce 3d_{5/2} and Pt 4d_{5/2} BEs, and Ce(III)/Ce and Br/(Ce + Al) surface atomic ratios are reported in Table 3, and Fig. 9 shows the wide survey profile and

Table 3Catalysts characterization by XPS of fresh and used Pt/30%CeO₂–Al₂O₃ after exposure to MB at 400 °C for 10 h and 275 °C for 7 h, and exposure to HBr at 250 °C for 7 h.

Sample	Ce 3d _{5/2} (eV)	Ce(III) (%)	Pt 4d _{5/2} (eV)	Br/(Ce + Al)
Fresh	884.0	22.1	316.0	0
400 °C–MB–10 h	882.8	16.8	315.4	0.021
275 °C–MB–7 h	883.6	8.0	315.8	0.023
250 °C–HBr–7 h	883.8	7.6	315.8	0.025

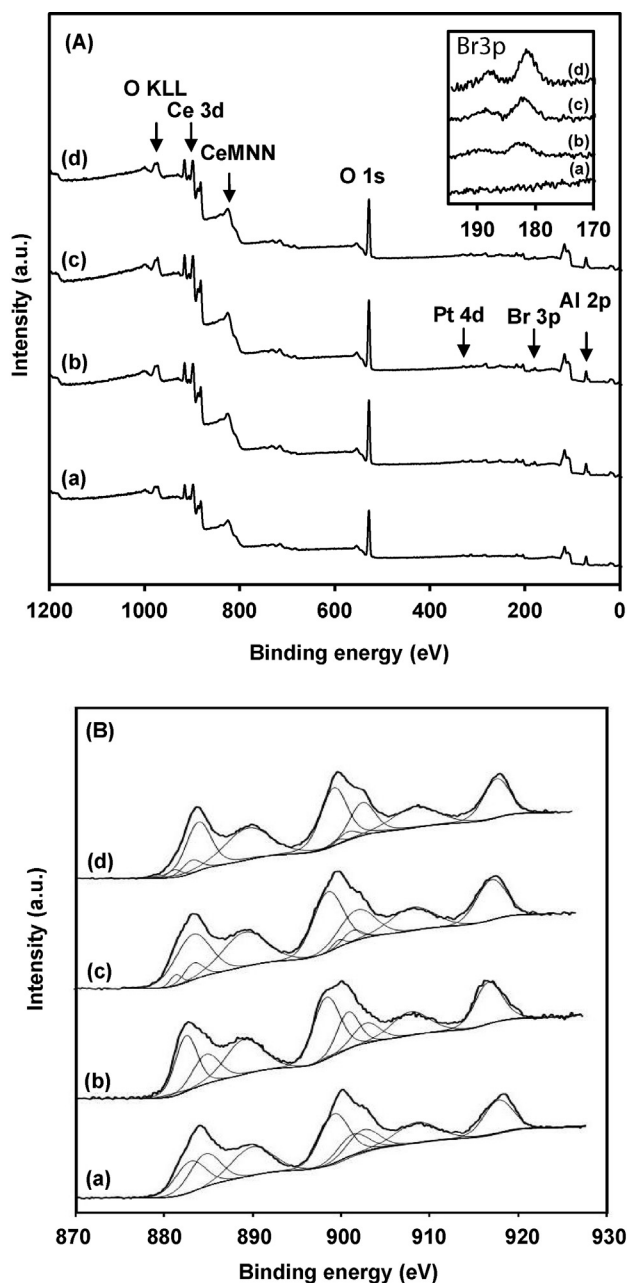


Fig. 9. (A) Wide survey and (B) core-level Ce 3d XPS spectra of Pt/30%CeO₂–Al₂O₃: (a) fresh, (b) after exposure to MB at 400 °C for 10 h, (c) 275 °C for 7 h, and (d) after exposure to HBr at 250 °C for 7 h.

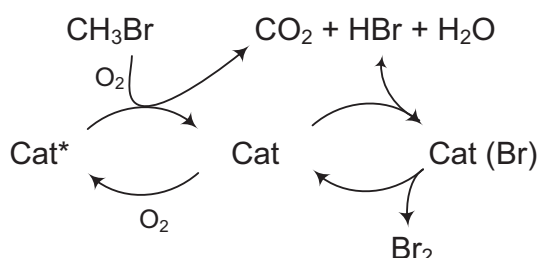


Fig. 10. Proposed pathway of catalytic oxidation of MB over synthesized CeO_2 -based combustion catalysts.

core-level Ce 3d XPS spectra. Pt 4d lines were analyzed instead of the most intense Pt 4f peak due to the overlap of the latter with Al 2p lines in the region of 70–80 eV. In all samples the BE values of Pt 4d_{5/2} (315.6–316.2 eV) are between the reported BE of Pt(0) (313.5 eV) and Pt(IV) (317.0 eV) [51], indicating an oxidized Pt species interacting with the ceria support. The complex Ce spectra, first resolved by Burroughs et al. [52], consist of two sets of spin-orbital multiples, corresponding to the 3d_{5/2} and 3d_{3/2} contributions. The deconvoluted peaks of Ce 3d spectra refer to Ce(III) (two pairs of doublets) and Ce(IV) (three pairs of spin-orbit doublets); semiquantitation of surface state of Ce can thus be obtained by integrating areas accordingly.

As shown in Table 3, the greater BE of Ce 3d_{5/2} and Ce 3d_{3/2}, relative to the value for bulk CeO_2 (881.8–882.4 eV) [53], for all the samples suggests electron transfer between CeO_2 and the alumina support, as well as between CeO_2 and Pt [54]. The major valence of Ce in all the tested samples is +IV, consistent with the XRD result. The presence of Ce(III) in all tested samples, even the fresh catalyst, is consistent with the findings of other studies of alumina-supported ceria [26,54,55]. Also it was reported that cerium in Pt/ CeO_2 - Al_2O_3 is in a more reduced state than the cerium in CeO_2 - Al_2O_3 samples without Pt [54]. Although Ce(III) can be an artifact of the XPS method [56], its formation was found to be negligible in crystalline samples irradiated for a short time (~15 min) [56], and the Ce(III) produced by photoreduction in any case should be the same for all samples because they came from the same catalyst batch and were analyzed under identical conditions. The 400 °C-MB-10 h catalyst contained a slightly lower but comparable Ce(III) concentration as the fresh catalyst, implying the Ce surface state remained stable after 10 h time-on-stream operation, which is consistent with Fig. 6. The Ce(III) concentration for 275 °C-MB-7 h and 250 °C-HBr-7 h samples are similar to each other and are lower than fresh and 400 °C-MB-10 h samples.

Table 3 shows no Br in the fresh sample but around 2% relative to (Ce + Al) in the used samples. The trend increases in the order 400 °C-MB-10 h < 275 °C-MB-7 h < 250 °C-HBr-7 h. This trend is consistent with the greater retention of Br on the catalyst when temperature decreases, as indicated by the incomplete recovery of Br in MB oxidation at lower temperature in Fig. 7 and the hysteresis of the HBr conversion curve in Fig. 8. Inspection of Table 3 shows that Br content decreases as Ce(III) content increases. This makes sense mechanistically if it is assumed that as the temperature increases more Br^- leaves as Br_2 simultaneous with Ce(IV) reduction to Ce(III). Analogously, in CO oxidation over CeO_2 -supported catalysts, more Ce(III) was produced as temperature increased due to the decomposition of a Ce(IV)-CO intermediate state [57].

Fig. 10 summarizes the oxidation pathway of MB over Pt/30% CeO_2 - Al_2O_3 . The lack of catalyst activity under nitrogen flow for 3 h at both 350 °C and 400 °C indicates that gas phase O_2 rather than bulk lattice oxygen contributes the most to catalyzed oxidation. By analogy with hydrocarbons, MB likely interacts with coordinatively unsaturated (“active”) lattice oxygen on the surface layer. The catalyst in activated form is designated

“cat*” in the Fig. 10. The interaction of MB with cat* leads to conversion of MB to CO_2 , H_2O and HBr through steps that cannot be addressed by our limited study. HBr is oxidized to Br_2 in a separate step. Water has little effect on MB oxidation but modestly suppresses HBr oxidation (Fig. 7). Water suppression of HBr oxidation is kinetic, not thermodynamic as implied by Eq. (9), again, because the Deacon-type reaction lies far to the right. Also, retention of Br^- on the catalyst at 300 °C is greater when the MB feed stream is humidified (Table 2). The exact role of water in HBr conversion remains speculative at this time.

4. Conclusions

This study reports catalytic oxidation of MB over Pt, Pd, Fe_2O_3 , CuO, or PbO nanoparticles on oxide (Al_2O_3 , SiO_2 , and TiO_2) or mixed-oxide (CeO_2 - Al_2O_3 , CeO_2 - SiO_2 , and CeO_2 - TiO_2) supports, and by self-assembled core-shell catalysts (Pd@ SiO_2 and Pd@10% CeO_2 - Al_2O_3). Ceria-based catalysts are far superior among the supports tested. The 1 wt% Pt/30% CeO_2 - Al_2O_3 completely oxidized MB at 400 °C, and was the most active catalyst tested, although 100% CeO_2 was nearly as active. Both HBr and Br_2 are produced and there is no evidence for bromate ion. Br was detected on the surface of used catalyst, and at a higher concentration at lower temperature, which is consistent with the greater retention of Br we observed on the catalyst when temperature decreases. Supportively, as the temperature increases, Ce(III) concentration increases and Br concentration decreases, due to more Br^- leaving as Br_2 simultaneous with Ce(IV) reduction to Ce(III). The selectivity for Br_2 increases with temperature and percent conversion of MB. Bromine is catalytically produced from HBr, the direct oxidation product of MB. This study shows that ceria-based catalysts such as 1 wt% Pt/30% CeO_2 - Al_2O_3 or 100% CeO_2 can be used for effective destruction of MB in air simulating vent streams from QPS chamber fumigations. Both Br_2 and HBr are easily scrubbed from the treated gas streams by conventional means for disposal or recovery. The catalyst may also be suitable for industrial production of Br_2 .

Acknowledgements

We acknowledge Dr. Spencer Walse, Dr. Michael Rooks, Dr. Stephen Golledge, Dr. William Schwartz, and Mr. Craig Musante for their assistance with methods and instrumental training, helpful discussions, and technical support throughout the system setup and analysis phases of the research. This project was funded by a FAS/U.S. Department of Agriculture TASC grant managed through the California Dried Plum Board.

Appendix A. Supplementary data

Supplementary data associated with this article can be found, in the online version, at <http://dx.doi.org/10.1016/j.apcatb.2013.06.019>.

References

- [1] J.B. Ristaino, W. Thomas, *Plant Disease* 81 (1997) 964–977.
- [2] The phase out of methyl bromide, US Environmental Protection Agency, <<http://www.epa.gov/ozone/mbr/>> (accessed May 2013).
- [3] Other regulatory information, US Environmental Protection Agency, <<http://www.epa.gov/ozone/mbr/otherreginfo.html>> (accessed May 2013).
- [4] Critical use exemption information, US Environmental Protection Agency, <<http://www.epa.gov/ozone/mbr/cueinfo.html>> (accessed May 2013).
- [5] Quarantine and pre-shipment (QPS) exemption, US Environmental Protection Agency, <<http://www.epa.gov/ozone/mbr/qpsinfo.html>> (accessed May 2013).
- [6] European Community Management Strategy for the phase-out of the critical uses of methyl bromide, United Nations Environment Programme, <<http://ozone.unep.org/Exemption.Information/Critical.use.nominations.for.methyl.bromide/MeBr.Submissions/EC%20Management%20Strategy%20for%20Methyl%20Bromide.pdf>> (accessed May 2013).

- [7] Methyl bromide—registration, import consent and bans, PAN Pesticide Database, Pesticide Action Network, North America, San Francisco, CA, <<http://www.pesticideinfo.org/Detail.ChemReg.jsp?Rec.Id=PC32864#working>> (accessed May 2013).
- [8] R.C. Xuan, D.J. Ashworth, L.F. Luo, S.R. Yates, *Environmental Science and Technology* 45 (2011) 2317–2322.
- [9] R.C. Xuan, D.J. Ashworth, L.F. Luo, H.Z. Wang, S.R. Yates, *Environmental Science and Technology* 44 (2010) 9080–9085.
- [10] J.G. Leesch, G.F. Knapp, B.E. Mackey, *Journal of Stored Products Research* 36 (2000) 65–74.
- [11] J.D. Snyder, J.G. Leesch, *Industrial and Engineering Chemistry Research* 40 (2001) 2925–2933.
- [12] J.Y. Gan, S.R. Yates, *Journal of Hazardous Materials* 57 (1998) 249–258.
- [13] G.W. Peterson, J.A. Rossin, P.B. Smith, G.W. Wagner, *Carbon* 48 (2010) 81–88.
- [14] R.A. Sheldon, R.A. Santen, *Catalytic Oxidation: Principles and Applications*, World Scientific Publishing Co. Pte. Ltd., Singapore, 1995.
- [15] K. Everaert, J. Baeyens, *Journal of Hazardous Materials* 109 (2004) 113–139.
- [16] D.M. Papenmeier, J.A. Rossin, *Industrial and Engineering Chemistry Research* 33 (1994) 3094–3103.
- [17] H. Windawi, Z.C. Zhang, *Catalysis Today* 30 (1996) 99–105.
- [18] G. Siquin, C. Petit, S. Libs, J.P. Hindermann, A. Kiennemann, *Applied Catalysis B: Environmental* 27 (2000) 105–115.
- [19] M. Wu, X.Y. Wang, Q.G. Dai, Y.X. Gu, D. Li, *Catalysis Today* 158 (2010) 336–342.
- [20] B. de Rivas, C. Sampedro, R. Lopez-Fonseca, M.A. Gutierrez-Ortiz, J.I. Gutierrez-Ortiz, *Applied Catalysis A: General* 417 (2012) 93–101.
- [21] Q.Q. Huang, X.M. Xue, R.X. Zhou, *Journal of Molecular Catalysis A: Chemical* 344 (2011) 74–82.
- [22] A. Trovarelli, *Catalysis Reviews – Science and Engineering* 38 (1996) 439–520.
- [23] Y. Nagai, T. Hirabayashi, K. Dohmae, N. Takagi, T. Minami, H. Shinjoh, S. Matsumoto, *Journal of Catalysis* 242 (2006) 103–109.
- [24] J.L. Duplan, H. Praliaud, *Applied Catalysis* 67 (1991) 325–335.
- [25] B. Harrison, A.F. Diwell, C. Hallett, *Platinum Metals Review* 32 (1988) 73.
- [26] M. Ousmane, L.F. Liotta, G. Di Carlo, G. Pantaleo, A.M. Venezia, G. Deganello, L. Retaillieu, A. Boreave, A. Giroir-Fendler, *Applied Catalysis B: Environmental* 101 (2011) 629–637.
- [27] C.H. Wang, S.S. Lin, C.L. Chen, H.S. Weng, *Chemosphere* 64 (2006) 503–509.
- [28] S. Pitkaaho, L. Matejova, S. Ojala, J. Gaalova, R.L. Keiski, *Applied Catalysis B: Environmental* 113 (2012) 150–159.
- [29] Z. Abbasi, M. Haghighi, E. Fatehifar, S. Saedy, *Journal of Hazardous Materials* 186 (2011) 1445–1454.
- [30] T.X.T. Sayle, S.C. Parker, C.R.A. Catlow, *Surface Science* 316 (1994) 329–336.
- [31] H.C. Yao, Y.F.Y. Yao, *Journal of Catalysis* 86 (1984) 254–265.
- [32] Y.F.Y. Yao, *Journal of Catalysis* 87 (1984) 152–162.
- [33] B.K. Hodnett, *Heterogeneous Catalytic Oxidation: Fundamental and Technological Aspects of the Selective and Total Oxidation of Organic Compounds*, John Wiley & Sons, Inc., New York, 2000.
- [34] D. Ciuparu, M.R. Lyubovsky, E. Altman, L.D. Pfefferle, A. Datye, *Catalysis Reviews – Science and Engineering* 44 (2002) 593–649.
- [35] A.P. Amrute, C. Mondelli, M.A.G. Hevia, J. Perez-Ramirez, *ACS Catalysis* 1 (2011) 583–590.
- [36] B. de Rivas, R. Lopez-Fonseca, C. Sampedro, J.I. Gutierrez-Ortiz, *Applied Catalysis B: Environmental* 90 (2009) 545–555.
- [37] R.A. van Santen, P.W.N.M. van Leeuwen, J.A. Moulijn, B.A. Averill, *Catalysis: An Integrated Approach*, Elsevier Science B.V., Amsterdam, 1999.
- [38] A.J. Forman, J.N. Park, W. Tang, Y.S. Hu, G.D. Stucky, E.W. McFarland, *ChemCatChem* 2 (2010) 1318–1324.
- [39] M. Cargnello, N.L. Wieder, T. Montini, R.J. Gorte, P. Fornasiero, *Journal of the American Chemical Society* 132 (2010) 1402–1409.
- [40] A.E. Greenberg, L.S. Clesceri, A.D. Eaton, *Standard Methods for the Examination of Water and Wastewater*, American Public Health Association, Washington, DC, 2012.
- [41] Z.E. Jolles, *Bromine and Its Compounds*, Ernest Benn Limited, London, 1966.
- [42] S. Saitzek, J.F. Blach, S. Villain, J.R. Gavarrí, *Physica Status Solidi A – Applications and Materials Science* 205 (2008) 1534–1539.
- [43] W.M. Haynes, *CRC Handbook of Chemistry and Physics*, 92nd ed., CRC Press/Taylor and Francis, Boca Raton, FL, 2012.
- [44] S. Utsunomiya, R.C. Ewing, *Environmental Science and Technology* 37 (2003) 786–791.
- [45] R. Maache, R. Brahmi, L. Pirault-Roy, S. Ojala, M. Bensitel, *Topics in Catalysis* 56 (2013) 658–661.
- [46] M. Cargnello, J.J. Delgado Jaén, J.C. Hernández Garrido, K. Bakhmutsky, T. Montini, J.J. Calvino Gómez, R.J. Gorte, P. Fornasiero, *Science* 337 (2012) 713–717.
- [47] J.R. Gonzalez-Velasco, A. Aranzabal, J.I. Gutierrez-Ortiz, R. Lopez-Fonseca, M.A. Gutierrez-Ortiz, *Applied Catalysis B: Environmental* 19 (1998) 189–197.
- [48] H. Deacon, Gaskell, Deacon and Co US patent 85370.1868.
- [49] A.P. Amrute, C. Mondelli, M. Moser, G. Novelli-Leruth, N. Lopez, D. Rosenthal, R. Farra, M.E. Schuster, D. Teschner, T. Schmidt, J. Perez-Ramirez, *Journal of Catalysis* 286 (2012) 287–297.
- [50] P.F. Schubert, R.D. Beatty, S. Mahajan, in: J.N. Armor (Ed.), *Environmental Catalysis*, American Chemical Society, Washington, 1994, pp. 405–419.
- [51] J.Z. Shyu, K. Otto, *Applied Surface Science* 32 (1988) 246–252.
- [52] P. Burroughs, A. Hamnett, A.F. Orchard, G. Thornton, *Journal of the Chemical Society: Dalton transactions* 17 (1976) 1686–1702.
- [53] J.F. Moulder, W.F. Stickle, P.E. Sobol, K.D. Bomben, *Handbook of X-ray Photoelectron Spectroscopy: A Reference Book of Standard Spectra for Identification and Interpretation of XPS Data*, Physical Electronics, Inc., Minnesota, 1995.
- [54] B.A. Riguetto, S. Damyanova, G. Gouliev, C.M.P. Marques, L. Petrov, J.M.C. Bueno, *Journal of Physical Chemistry B* 108 (2004) 5349–5358.
- [55] J.C. Serrano-Ruiz, G.W. Huber, M.A. Sanchez-Castillo, J.A. Dumesic, F. Rodriguez-Reinoso, A. Sepulveda-Escribano, *Journal of Catalysis* 241 (2006) 378–388.
- [56] P.W. Park, J.S. Ledford, *Langmuir* 12 (1996) 1794–1799.
- [57] A. Martinez-Arias, M. Fernandez-Garcia, O. Galvez, J.M. Coronado, J.A. Anderson, J.C. Conesa, J. Soria, G. Munuera, *Journal of Catalysis* 195 (2000) 207–216.